Integration of DC Microgrids as Virtual Synchronous Machines Into the AC Grid

Dong Chen, Yizhe Xu, *Student Member, IEEE*, and Alex Q. Huang, *Fellow, IEEE*

***Abstract*—A smart and autonomous integration concept for dc microgrids into the legacy ac grid is proposed based on the virtual synchronous machine (VSM) concept. It utilizes a dc–ac converter as a universal VSM-based interface (VSMBI) between the ac grid and various distributed energy resources (DER) connected on the dc side. The control strategy of it includes: 1) a frequency regulation improved from previous VSM works, which is suitable for the microgrid integration; 2) an improved dual droop control between the ac frequency and the dc side energy storages; 3) a power system stabilizer to enhance the system stability. Under this concept, the VSMBI integrates the DERs, loads and energy storages in the dc microgrid into a VSM. The VSMBI and the dc microgrid together will respond to short-term and long-term requirements of the grid frequency regulation, and achieve autonomous power management for the ac grid and the dc microgrid. It is therefore an important step forward in supporting high DER penetration. The concept, its design and small-signal analysis are presented in this paper. Its effectiveness and functions are verified by simulation and experimental results.**

***Index Terms*—dc microgrids, distributed energy resources (DER), droop control, power management, stability, virtual synchronous machine (VSM).**

I. Introduction

With the rapid growth of renewable and distributed energy resources (DER), their impact on the legacy ac grid is becoming an important topic. Among integration strategies, dc microgrid is attractive because of the high efficiency and simple dc interface for various DERs and energy storages. When connected to the ac grid, it utilizes a dc–ac converter as the interface. However, there are still many major challenges to integrate dc microgrids in the legacy power system.

1) dc–ac converters using traditional power electronics control strategy have fast dynamics. However, the key equipment in power system: the synchronous machine (SM), has slow dynamics with large inertia. The equivalent rotational inertia of the grid will significantly decrease at high DER penetration. This will cause degradation in frequency stability.
2) The power generated by DERs is intermittent, and will be instantly presented to the grid through fast responding dc–ac converters. These interactions will lead to frequency, angle, and voltage instability [1]. The investigation is also hard for large-scale dc microgrids and dc–ac converters in parallel [2], especially when the DERs have similar dynamics with the dc–ac converters. Meanwhile, DERs usually work under the maximum power point tracking (MPPT) control and thus are nondispatchable. So these dc–ac converters cannot provide up-reserve to support the grid frequency.
3) Under all grid conditions, the ac frequencies, voltages of ac grids, and the dc voltages of dc microgrids should be controlled within a safe operation range. Autonomous controls are necessary for the dispatchable units, such as the energy storages in the dc microgrid and the dc–ac converters, to achieve power balancing and sharing.

Today, the dc–ac converters lack rotational inertia and do not interact with the grid like the SMs. To solve these problems, dc–ac converters mimicking SMs are proposed [3]–[12]. These virtual synchronous machines (VSM) offer several benefits.

1) A much larger inertia than traditional dc–ac converters is introduced [11].
2) Their models are simple hence promising for studying scalability and stability of paralleled VSMs.
3) The use of phase lock loop (PLL) is eliminated during normal operation, since the VSMs can synchronize with the grid based on the power balance [7]
4) Seamless transition from grid-connecting mode to islanding mode and resynchronization back with the grid as a voltage source [5].

However, most of previous works on VSMs are under the assumption that there is an ideal source on the dc side [4]–[12]. This is reasonable in the early stage of VSM works to focus on the ac side emulation. In [5]–[7], the VSMs control the output active power according to the ac frequency, and provide up-reserve, down-reserve to the grid via traditional droop algorithm. But in steady state, they can only output a fixed power for a given ac frequency. When the DERs and loads with intermittent and variable powers are connected, additional controls will be needed for the DERs and loads. A frequency and angle regulation is used in [3] to control both the ac frequency and dc voltage. This VSM can operate in inverter or rectifier mode without reconfiguration. However, it can only work at a rated ac frequency and dc voltage, due to the use of an integrator in its

Manuscript received August 16, 2016; revised October 29, 2016 and November 28, 2016; accepted December 13, 2016. Date of publication February 24, 2017; date of current version August 9, 2017.

The authors are with the Department of Electrical and Computer Engineering, North Carolina State University, Raleigh, NC, 27695 USA (e-mail: cedee128@gmail.com; yxu10@ncsu.edu; aqhuang@ncsu.edu).

Color versions of one or more of the figures in this paper are available online at http://ieeexplore.ieee.org.

Digital Object Identifier 10.1109/TIE.2017.2674621

control loop. Thus it cannot react to variable ac frequencies to provide long-term reserves.

Droop control is widely used in power system to support the grid frequency and voltage. In microgrids, it is also a popular autonomous control to achieve power sharing among paralleled units [13]–[19]. The droop method in [18] and [19] controls the ac side's frequency and the dc side's voltage of the dc–ac converter to the same point along the ac frequency droop slope and the dc voltage droop slope, which is suitable for interlinking the ac subgrids and dc subgrids. For multiple-layer systems in practical application with volatile DERs, ac grids and dc microgrids in different layers need to achieve power management. Hierarchical droop control with coordination between the ac grids and dc microgrids should be considered.

This paper proposes a dc microgrid integration concept to address above mentioned issues. It controls the dc–ac converter as a VSM-based interface (VSMBI), and includes the following:

1) a frequency regulation improved from [3], but enables the ac frequency and dc voltage being regulated within desired ranges;
2) an improved dual droop control separately for the VSMBI and the dc side energy storages to support the VSM functions and achieve the power management;
3) an additional power system stabilizer (PSS) to enhance the system stability.

Under this concept, the VSMBI integrates the DERs, loads, and energy storages in the dc microgrid into a VSM from the grid point of view. The VSMBI and the dc microgrid together will introduce inertia during the ac side and dc side dynamics, and provide up-reserve and down-reserve in steady state to the grid. These VSM functions are supported by practical dc side energy storages through the dual droop control. Improved from previous VSMs, the power balancing and sharing in the ac grid and dc microgrid are simultaneously achieved under different grid conditions and in an autonomous and distributed fashion. Moreover, the DERs and loads connected to the VSMBI can output any power in steady state, according to their characteristics such as the MPPT control. During the dynamics, the intermittent and variable powers from the DERs and loads are slowed, and the VSMBI's ac output dynamics is decoupled from the dc side. Thus the system model of the VSMBI and the dc microgrid under this concept is simple, and promising for studying scalability and stability of paralleled systems. Due to the grid support capabilities similar to the SMs, the concept is a smart, autonomous, and flexible solution to support high DER penetration in today's power grid.

II. VSM Interfaced DC Microgrids

Fig. 1 shows the overall architecture of the VSMBI and the dc microgrid with the control strategy. A dc–ac converter is used as the VSMBI. Battery-based energy storage units and photovoltaic (PV) based DER units are considered in the dc microgrid, and each unit contains a corresponding dc–dc converter. Different kinds of circuit topologies can be adopted for the dc–dc converter in the energy storage units and DER units, and the options depend on the voltages, power ratings, insulations, etc. The detailed topology of the dc–dc converter is not discussed in this paper, because it is not our focus. In Fig. 1, wide arrows show the power flows: P_{out} and Q are the VSMBI's output active and reactive power, P_{in} is the input power from the dc microgrid, and P_{bat}, P_{PV}, and P_{load} are the power of battery unit, PV unit, and load, respectively.

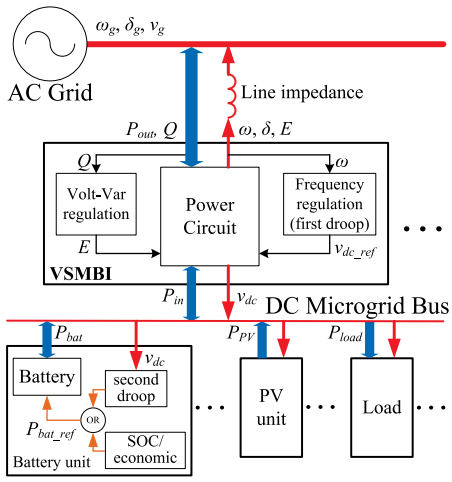

Fig. 1. Overall architecture of the VSMBI and the dc microgrid with the control strategy.

A. VSM-Based Interface

The traditional SM rotor's mechanical characteristic is called swing equation [20] and expressed as [3], [7]

$$J\frac{d\omega_r}{dt} + D(\omega_r - \omega_g) = T_m - T_e \tag{1}$$

where ω_r is the rotor angular frequency, ω_g is the grid frequency, J is the angular momentum inertia of the rotor, D is the damping coefficient generated by the damper windings, and T_m and T_e are the input mechanical torque and load electric torque, respectively. The dynamics of SM rotor is determined by J and is very slow. In the power system analysis, the frequency and angle stability are also mainly based on (1).

Fig. 2(a) shows the power circuit of the VSMBI, which contains a full bridge, a LCL filter, and a dc capacitor, as used in traditional dc–ac converter [7]. Fig. 2(b) shows the detailed control strategy of the VSMBI, improved from previous VSMs and droop controls [3]–[17]. It uses the filter capacitor (C_f) voltage v_C, the filter inductor (L_f) current i_L, and the dc voltage v_{dc} as the feedback variables, and controls the ac voltage angular frequency ω, angle δ, amplitude E, and v_{dc}, to emulate the SM's characteristic in (1). In Fig. 2(b), ω_R, E_R, v_{dc_R}, and Q_R are the rated values of ω, E, v_{dc}, and Q, respectively. Three first-order low-pass filters (LPF) are used, their corner frequencies are ω_{c1}, ω_{c2}, and ω_{c3}, respectively. Among them, $G_{LPF1}(s)$ and $G_{LPF2}(s)$ are used to suppress the low-order harmonics for v_{dc} and Q, and filter them to v_{dc_f} and Q_f, respectively. Here the VSMBI works as a voltage source based on its own ω, δ, and E [21], which are different from the grid voltage angular frequency ω_g, angle δ_g, and amplitude v_g in Fig. 1.

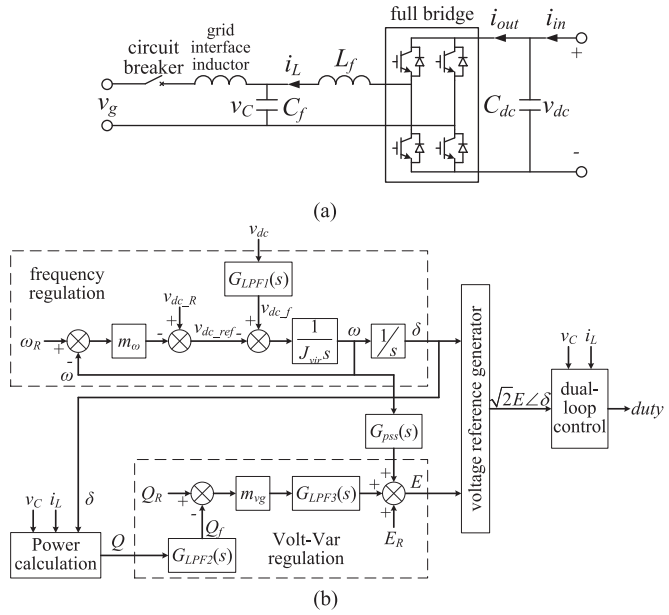

Fig. 2. Detailed diagram of the VSMBI: (a) power circuit and (b) control strategy.

In this paper, a single-phase ac system is adopted as an example although the proposed concept also applies to three-phase ac systems.

In Fig. 2(b), the ac voltage reference is generated by the frequency regulation and Volt–Var regulation together. The VSMBI's ac output voltage is controlled to follow it by a traditional power electronics dual-loop control, which contains an outer loop for v_C (also the VSMBI's ac output voltage) and an inner loop for i_L [7]. Powers P_{out} and Q are also calculated from v_C and i_L based on the VSMBI's own δ. If lower switching frequency is used in the VSMBI, the power electronics control may interact with the frequency and Volt–Var regulations [22]. In this paper, a much higher switching frequency than ω_g is used, thus the power electronics control is much faster than the two regulations. The VSMBI is assumed to follow the ac voltage reference without any delay.

1) Frequency Regulation: The dynamic equation of the dc voltage with a dc capacitor C_{dc} can be revised as [3]

$$C_{dc}v_{dc}\frac{dv_{dc}}{dt} = i_{in}v_{dc} - i_{out}v_{dc} = P_{in} - P_{out} \qquad (2)$$

where i_{in} is the current from the dc microgrid into C_{dc}, and i_{out} is the current from C_{dc} into the full bridge, as shown in Fig. 2(a). Equation (2) is similar with (1), where $C_{dc}v_{dc}$, v_{dc}, P_{in}, and P_{out} into the VSMBI are, respectively, corresponding to J, ω_r, T_m, and T_e. Assuming the VSMBI is lossless, P_{out} is also the output active power into the ac grid. Equation (3) shows the dc capacitor has the similar function with the SM rotor, and can be used for the inertia emulation in VSMs [3], [10]. But to get the same inertia as a SM rotor, the dc capacitor will be very large.

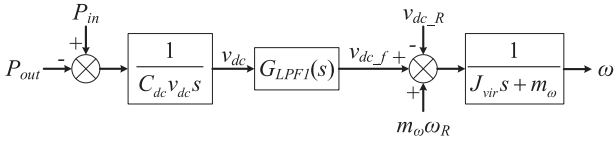

Fig. 3. Block diagram of the VSMBI's virtual rotor model.

The equation of the frequency regulation in Fig. 2(b) is

$$J_{vir}\frac{d\omega}{dt} + m_\omega(\omega - \omega_R) = G_{LPF1}(s)v_{dc} - v_{dc\_R}. \qquad (3)$$

Equation (3) is also similar with (1), where the virtual inertia parameter J_{vir} and damping coefficient m_ω are, respectively, corresponding to J and D. So this regulation can also emulate the SM rotor's characteristic without physical component. The difference is that the torque is replaced by v_{dc}, and the dynamic (2) is then inserted in the swing equation.

Equations (2) and (3) are the VSMBI's virtual rotor model and mimic the swing characteristic. Its block diagram is shown in Fig. 3 in s-domain. When P_{in} or P_{out} varies, the difference between them will change v_{dc} based on C_{dc}, and then ω based on J_{vir}. This will change δ and then P_{out} according to the power-angle relationship [20]. Finally, a new balanced working point for P_{in}, P_{out}, and δ is reached, while ω synchronizes with ω_g again [3], [20]. The VSMBI's total inertia is determined by C_{dc}, v_{dc}, ω_{c1}, and J_{vir}. When C_{dc} is designed normally, J_{vir} will be an extra control parameter to adjust the inertia to meet the stability requirement in the power system.

According to the analysis above, any power from the dc microgrid can be transmitted to the ac grid through the VSMBI at a given ac frequency [3]. The dynamics of ac output active power is slowed down and completely decoupled from the intermittent, variable DERs and loads in the dc microgrid. So this VSMBI's model is simple and promising for studying scalability and stability of paralleled systems. Due to its swing characteristic, the VSMBI is able to respond to the short-term requirements of the grid frequency regulation [20].

2) Improvement in Frequency Regulation: In (3), m_ω emulates the damping coefficient, which can be achieved in different ways [7], [12]. Improved from the VSM in [3], the angle loop with an integrator is eliminated, and m_ω is designed based on the allowable variations in ac frequency and dc voltage in this paper. While keeping the benefits mentioned above, the VSMBI will be able to operate in certain ranges of ω and v_{dc}. This improvement is the prerequisite, both for the VSMBI to respond to the grid frequency regulation requirements by autonomous controls of energy storages, and for the microgrid integration and system power management. The method to achieve these will be described in Section II-B.

Indeed, m_ω is also the $\omega - v_{dc}$ droop slope. Its implementations are different from the traditional ω-P (angular frequency to active power) droop, which can be utilized separately from the damping coefficient [6]–[8]. It is different from the dc voltage to inverter's internal current droop in [17] either. Typically, m_ω is much smaller than that in [3]. Its damping effect is degraded

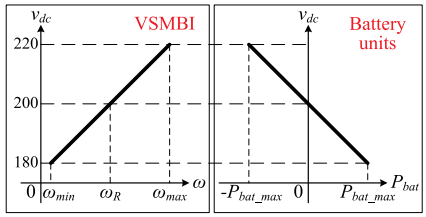

Fig. 4. Detailed diagram of dual droop control.

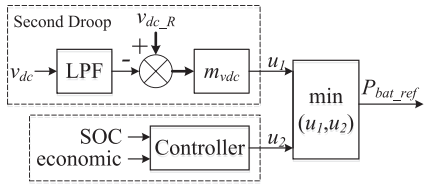

Fig. 5. Detailed control diagram of battery-based energy storage units.

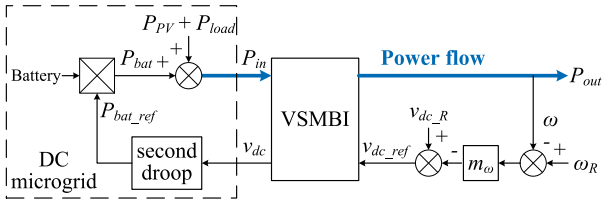

Fig. 6. Coordination diagram of dual droop control.

[20], [23]. The analysis of the system stability and additional improvement methods will be discussed in Section III.

3) Volt–Var Regulation: In Fig. 2(b), a simple *V-Q* (voltage to reactive power) droop control is adopted to mimic the excitation system of SMs [3]–[5], where m_{vg} is its droop slope. In SMs, the exciter is usually a proportional controller, and the field circuit flux is produced based on it after a long-time delay [20]. To emulate this, a first-order LPF can be adopted, shown as $G_{LPF3}(s)$ in Fig. 2(b). In this paper, ω_{c3} is chosen to be the same with ω_{c1}, much larger than that in the excitation system of SMs.

B. Dual Droop Control

To support the demanded inertia in practical applications, storage units such as battery with a dc–dc converter should be considered, and they have several additional benefits compared with just connecting a large capacitor bank to the dc bus.

To achieve the power management under different grid conditions, the droop control is adopted. However, if ω-*P* and *V-P* (dc voltage to active power) droop controls are independently and separately adopted in the ac grid and the dc microgrid, the power from them will be unbalanced and uncoordinated. To overcome this problem, an improved dual droop control for the VSMBI and the energy storage units is proposed, as shown in Fig. 1, and Fig. 4 shows the details.

1) First Droop in VSMBI: Since the energy storage units in the dc microgrid only react to v_{dc}, ω in the VSMBI must be linked to v_{dc} through the active power. The traditional droop controls for active power in ac and dc system, respectively, are

$$\omega - \omega_R = -k_\omega(P - P_{rate}) \tag{4}$$

$$v_{dc} - v_{dc\_R} = -k_{vdc}(P - P_{rate}) \tag{5}$$

where P_{rate} is the converters' rated power, and k_ω and $k_{v\ dc}$ are the droop slopes for ac and dc system. Combining (4) and (5), the first droop in the VSMBI can be rewritten as

$$v_{dc} - v_{dc\_R} = \frac{k_{vdc}}{k_\omega}(\omega - \omega_R) = m_\omega(\omega - \omega_R). \tag{6}$$

In (6), m_ω is determined by the allowable ranges of ω and v_{dc}. Typically, $1/k_\omega$ is proportional to the VSMBI's rated power. In this paper, the dc voltage ranges are designed to be the same for different VSMBIs, then $1/k_{v\ dc}$ is also proportional to their rated power, and the resulting m_ω will be the same for different VSMBIs [24]. When the frequency regulation is improved to the one in Fig. 3, this droop control is naturally integrated in it, and m_ω is also the coefficient for part of the damping effect.

2) Second Droop in Energy Storage Units: The second droop in energy storage units is a traditional *V-P* droop, and m_{vdc} is its droop slope. According to the first droop in the VSMBI, P_{bat} should be controlled based on v_{dc}. This control is shown in the right column in Fig. 4, and Fig. 5 shows the detailed control diagram [24]. The state-of-charge (SOC) control and economic dispatch control are also shown. They are assumed not working in the following discussions since it is beyond our work.

3) Coordination of Dual Droop: To integrate the dc microgrid with the VSMBI into a VSM from the ac grid point of view, the dual droop is proposed as a hierarchical control. The system is also in a hierarchical architecture, where the ac grid is the upper layer, and the dc microgrid is the lower layer. Fig. 6 shows the coordination diagram of the dual droop control. In this paper, the PV units are under the MPPT control without power curtailment. In Fig. 6, the VSMBI always takes charges and regulates the lower-layer variable v_{dc} according to the upper-layer variable ω through the first droop, which is the upper-layer control. This voltage acts as a command, and tells the energy storage units how much power the VSMBI needs. Then energy storage units will output corresponding power through the second droop, which is the lower-layer control, and inject the power into the ac grid via the VSMBI. This is similar to the traditional active power control in SM [20], and finally the VSMBI with the dc microgrid will have the ω-*P* droop characteristic. The total ω-*P* droop slope is $m_\omega * (m_{vdc1} + m_{vdc2} + \ldots)$ when multiple energy storage units are connected to the VSMBI.

This dual droop control is distributed and autonomous without communication. In steady state, VSMBIs connected to the same ac grid will synchronize with it, share and balance the power according to the ac frequency, by commanding practical energy storages under each VSMBI via the dc voltage. So the VSMBI can provide up-reserve and down-reserve to the grid when ω_g varies in a desirable region. The power in the dc

TABLE I
PARAMETERS OF PROPOSED SINGLE-MACHINE INFINITE BUS SYSTEM

Symbol	Quantity	Value
f_s	switching frequency	10.8 kHz
C_{dc}	dc capacitor	4 mF
P_{rate}	Power rating	1200 W
ω_R	rated ac voltage angular frequency	120π rad/ s
E_R	rated ac voltage amplitude	120 VAC
v_{dc_R}	rated dc voltage	200 VDC
Q_R	rated reactive power	0 VA
J_{vir}	virtual inertia parameter	1.06
m_ω	damping coefficient / ac angular frequency to dc voltage droop slope	31.83
X	Sum of VSMBI's grid interface reactance and line reactance	10 mH
$\omega_{c1}, \omega_{c2}, \omega_{c3}$	corner frequency of LPFs	60π rad/ s
m_{vdc}	dc voltage to active power droop slope	25
K_{STAB_max}	maximum gain of power system stabilizer	30
T_w	time constant of high-pass filter	0.6366
T_1	time constant for phase lead	0.1592
T_2	time constant for phase lag	0.03183

microgrid under one VSMBI is also shared and balanced based on the second droop among paralleled energy storage units. So the power management of the ac grid and dc microgrid are achieved simultaneously in grid-connecting or islanding modes. During the dynamics, the dual droop control will also support the demanded inertia at a given ω_g. It is achieved in a similar way, by commanding energy storages to provide temporary energy to the VSMBI via v_{dc}, when ω varies due to the disturbances.

So the integration of the DERs, loads, and energy storages in the dc microgrid into a VSM from the ac grid point of view is achieved. The VSMBI with the dc microgrid can respond to both long-term and short-term requirements of the grid frequency regulation as a SM. Besides the basic VSM functions as in previous VSM studies, first, practical DERs and loads are connected to the VSMBI's dc side. They can output any power in steady state, due to the improvement in the frequency regulation. Meanwhile, the VSMBI's ac output is decoupled from them during the dynamics; and second, the VSM functions are supported by practical energy storages and the power management for the ac grid and dc microgrid is achieved, through the proposed dual droop control. Thus, the proposed concept is a smart and flexible way to integrate a higher penetration level of DERs into the ac grid than current practice.

III. SMALL-SIGNAL MODELING AND ANALYSIS

The small-signal model for a single-machine infinite bus system with one VSMBI, one battery unit, one PV unit, and one load is developed under the proposed concept. The system configuration is the same with Fig. 1. It is used for the analysis, simulations, and experiments in this paper. The research on such a system are fundamental in power system, and preliminary for paralleled-machine systems [20]. The dc microgrid interaction is studied and an additional regulator is introduced to enhance the stability. Table I summarizes the default parameters of the studied system. $m_\omega = 31.83$ is chosen so that v_{dc} works from 180 to 220 V [25], when ω works from 59.9 to 60.1 Hz; $m_{vg} = 0.005$ is chosen so that E works from 114 to 126 V when the VSMBI provides 100% to –100% reactive power to the grid.

A. Modeling and Analysis of the VSMBI

From (2) and Fig. 2(b), when the regulator $G_{pss}(s)$ is excluded, the original small-signal model of the VSMBI is given as

$$s\Delta E = -\omega_{c3}\Delta E - m_{vg}\omega_{c3}\Delta Q_f \tag{7}$$

$$s\Delta\delta = \Delta\omega \tag{8}$$

$$s\Delta\omega = \frac{1}{J_{vir}}\Delta v_{dc\_f} - \frac{m_\omega}{J_{vir}}\Delta\omega \tag{9}$$

$$s\Delta v_{dc} = \frac{1}{C_{dc}V_{dc}}\Delta P_{in} - \frac{1}{C_{dc}V_{dc}}\Delta P_{out} \tag{10}$$

$$s\Delta v_{dc\_f} = -\omega_{c1}\Delta v_{dc\_f} + \omega_{c1}\Delta v_{dc} \tag{11}$$

$$s\Delta Q_f = -\omega_{c2}\Delta Q_f + \omega_{c2}\Delta Q. \tag{12}$$

For the single-machine infinite bus system, ΔP_{out} and ΔQ based on the power-angle relationship are separately given as

$$\Delta P_{out} = \frac{2RE_0 - RV_g\cos\delta_0 + XV_g\sin\delta_0}{R^2+X^2}\Delta E + \frac{RE_0V_g\sin\delta_0 + XE_0V_g\cos\delta_0}{R^2+X^2}\Delta\delta = K_{PE}\Delta E + K_{P\delta}\Delta\delta \tag{13}$$

$$\Delta Q = \frac{2XE_0 - XV_g\cos\delta_0 - RV_g\sin\delta_0}{R^2+X^2}\Delta E + \frac{XE_0V_g\sin\delta_0 - RE_0V_g\cos\delta_0}{R^2+X^2}\Delta\delta = K_{QE}\Delta E + K_{Q\delta}\Delta\delta \tag{14}$$

where V_{dc}, V_g, E_0, and δ_0, respectively, are the steady-state values of v_{dc}, v_g, E, and δ, X is the sum of the VSMBI's grid interface reactance and line reactance, and R is the line resistance.

Fig. 7 shows the overall block diagram for the small-signal model of the VSMBI and the dc microgrid from (7)–(14) and Fig. 2(b) with the additional regulator $G_{pss}(s)$, where $G_{P\_dcmg}(s)$ is the power characteristics of the dc microgrid. This diagram is quite similar to that of the SM [20]. The differences are that, the dynamic (2) is inserted in the swing equation, and the excitation system is mimicked by the Volt–Var regulation.

In low-voltage distribution systems, R usually cannot be ignored. Virtual line impedance method [7] could be used to enhance the system performance. To simplify the analysis, pure inductive line impedance is assumed in the following discussions. It is also a typical case in power system [20], and corresponding to the droop controls and emulated swing characteristic in this paper. Then (13) and (14) can be simplified, and when δ_0 is nearly zero, from them there is

$$K_{PE}K_{Q\delta} \ll K_{P\delta}K_{QE}. \tag{15}$$

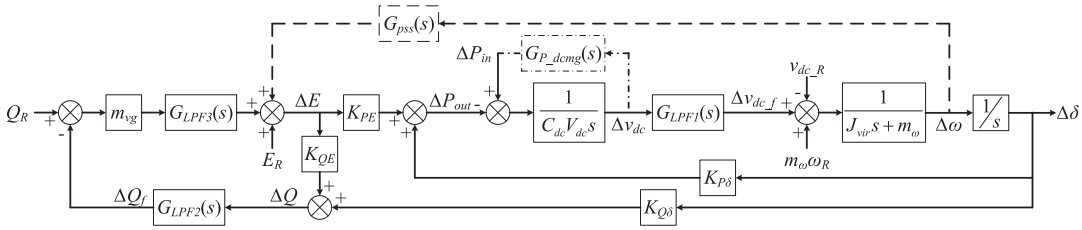

Fig. 7 . Overall block diagram for the small-signal model of the VSMBI and the dc microgrid.

From (7)–(15) and Fig. 7, the transfer function from ΔP_{in} to $\Delta\omega$ without $G_{pss}(s)$ and $G_{P\_dcmg}(s)$ can be derived as

$$\frac{\Delta\omega}{\Delta P_{in}} = \frac{G_{LPF1}(s)s}{C_{dc}V_{dc}s(J_{vir}s+m_\omega)s + G_{LPF1}(s)K_{P\delta}}. \quad (16)$$

In (16), larger J_{vir} and $K_{P\delta}$ will cause the system less stable. When the VSMBI outputs zero active power, δ_0 will be zero, $K_{P\delta}$ will reach its maximum value based on (13). The order of the characteristic equation in (16) is three, one order higher than that of the traditional SM [20]. Thus, to support large inertia at worst conditions, advanced method is necessary.

B. DC Microgrid Interaction

As discussed above, the dynamics of P_{out} is slowed down, and decoupled from P_{PV} and P_{load}. However, the fast responding P_{PV}, P_{load}, and P_{bat} still have influences on the VSMBI. Since the dynamics of these units are much faster than the frequency regulation in the VSMBI, their equations can be expressed as

$$P_{PV} = \text{constant}, P_{load} = -\frac{1}{R_{load}}v_{dc}^2,$$
$$P_{bat} = m_{vdc}(v_{dc\_R} - v_{dc}). \quad (17)$$

So the small-signal form of $G_{P\_dcmg}(s)$ will be revised as

$$G_{P\_dcmg}(s) = \frac{\Delta P_{in}}{\Delta v_{dc}} = \frac{\Delta P_{PV} + \Delta P_{load} + \Delta P_{bat}}{\Delta v_{dc}}$$
$$= -\frac{2V_{dc}}{R_{load}} - m_{vdc}. \quad (18)$$

Modeling the VSMBI from (7)–(15) with $G_{P\_dcmg}(s)$, and choosing one of the rated values as the input variable, v_{dc_R} for example, then the transfer function can be derived as

$$\frac{\Delta\omega}{\Delta v_{dc\_R}} = \frac{-[C_{dc}V_{dc}s - G_{P\_dcmg}(s)]s}{[C_{dc}V_{dc}s - G_{P\_dcmg}(s)](J_{vir}s+m_\omega)s + G_{LPF1}(s)K_{P\delta}}. \quad (19)$$

In (19), when $G_{P\_dcmg}(s)$ is negative, the system stability of the VSMBI with the dc microgrid will be enhanced, since the quadratic and linear coefficients in the characteristic equation of (19) are enlarged. If only constant current source is connected in the dc microgrid, $G_{P\_dcmg}(s)$ will be positive, and the stability will be degraded, since these two coefficients are reduced. If only PV units are connected, $G_{P\_dcmg}(s)$ will be zero, the stability will be the same with the original VSMBI model.

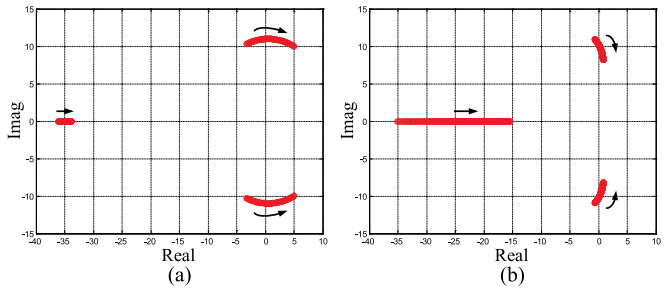

Fig. 8. Locus of the first three dominant eigenvalues for the system model with $G_{P\_dcmg}(s)$ and without $G_{pss}(s)$: (a) $-10 < G_{P\_dcmg}(s) < 5$, $J_{vir} = 1.06$; (b) $1.06 < J_{vir} < 4.24$, $G_{P\_dcmg}(s) = -5$.

There are six eigenvalues for the system model from (7)–(15) and (18). Fig. 8 shows the locus of the first three dominant eigenvalues when the VSMBI outputs zero power. To support the default virtual inertia J_{vir} in Table I, $G_{P\_dcmg}(s)$ should be smaller than –4.06 in Fig. 8(a); if $G_{P\_dcmg}(s) = -5$, the limitation for J_{vir} is 1.5, to maintain the system stable in Fig. 8(b). Since the loads could be zero, the energy storage units will take all the responsibility for the stability at this condition, and the minimum value of m_{vdc} can be calculated from the system model. This is the requirement on the m_{vdc} design in the proposed concept, based on the stability analysis. In this paper, $m_{vdc} = 25$ is chosen as an example, to keep the system stable even when a fully rated, positive current source is connected to the dc microgrid. If larger m_{vdc} is chosen, the system will be more stable, at the cost of larger power rating energy storage units.

In additional to supporting the functions and benefits as mentioned in Section II-B, the energy storage units also have the damping effect to enhance the stability in the proposed concept. The system needs one or some energy storage units (with total power rating larger than the minimum value) connected to the VSMBI. These energy storage units could be considered as part of the dc microgrid, while it is better to consider them as part attached to the VSMBI in the proposed concept, distinguished with the traditional energy storage applications. When energy storages with other controls are connected to the VSMBI as in traditional dc microgrid setup, they will be seen as normal sources or loads.

To keep the system's functions and stability even when all of the energy storage units in the proposed concept are working in SOC/economic mode, the rated dc voltage v_{DC_R} in Fig. 5 can be replaced by the SOC/economic command, which will be an

offset for the energy dispatching. The system still works with the dual droop control, and this part will be a future work.

C. Power System Stabilizer

In power system, PSS is used to add damping to the SM rotor oscillations by controlling its excitation using stabilizing signals, while this stabilizer must produce an electrical torque in phase with the rotor frequency changes [20]. In this paper, a regulator similar to the PSS is newly introduced to enhance the system stability, shown as $G_{pss}(s)$ in Fig. 2(b), although it also applies to any other VSMs. Since E in the VSMBI can be directly regulated, this regulator's result is directly added to E; and ω is used as the stabilizing signal. Its equation is given as

$$G_{pss}(s) = K_{STAB}\frac{sT_w}{1+sT_w}\frac{1+sT_1}{1+sT_2} \tag{20}$$

where K_{STAB} is the gain of $G_{pss}(s)$, T_w is the time constant of first-order high-pass filter, and T_1 and T_2 are the time constants for phase compensation. In this paper, typical values in [20] are adopted for T_w, T_1, and T_2. Let

$$E_{s1} = \frac{1+sT_1}{1+sT_2}E_{s2}, \quad E_{s2} = K_{STAB}\frac{sT_w}{1+sT_w}\omega. \tag{21}$$

The small-signal form of E_{s2} and E_{s1} will, respectively, be

$$s\Delta E_{s2} = -\frac{1}{T_w}\Delta E_{s2} + \frac{K_{STAB}}{J_{vir}}\Delta v_{dc\_f} - \frac{K_{STAB}m_\omega}{J_{vir}}\Delta\omega \tag{22}$$

$$s\Delta E_{s1} = -\frac{1}{T_2}\Delta E_{s1} + \frac{T_w - T_1}{T_2T_w}\Delta E_{s2} + \frac{T_1K_{STAB}}{T_2J_{vir}}\Delta v_{dc\_f} - \frac{T_1K_{STAB}m_\omega}{T_2J_{vir}}\Delta\omega. \tag{23}$$

After adding E_{s1} to E, (7) will be revised as

$$s\Delta E = -\omega_{c3}\Delta E - m_{vg}\omega_{c3}\Delta Q_f + \frac{T_2\omega_{c3}-1}{T_2}\Delta E_{s1} + \frac{T_w - T_1}{T_2T_w}\Delta E_{s2} + \frac{T_1K_{STAB}}{T_2J_{vir}}\Delta v_{dc\_f} - \frac{T_1K_{STAB}m_\omega}{T_2J_{vir}}\Delta\omega. \tag{24}$$

Equations (8)–(15), (18), and (22)–(24) give out the final overall small-signal model of the VSMBI and the dc microgrid with $G_{pss}(s)$. The transfer function can be derived as (25), shown at the bottom of the page, where

$$K_{pss} = \frac{K_{PE}G_{LPF1}(s)}{1 + G_{LPF3}(s)m_{vg}G_{LPF2}(s)K_{QE}}. \tag{26}$$

In (25), $G_{P\_dcmg}(s)$ has the most significant damping effect on the system, because it can change the quadratic and linear coefficients in the characteristic equation. $G_{pss}(s)$ is the second most significant, since it is placed in the linear term.

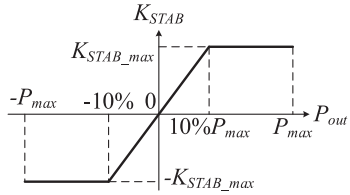

Fig. 9. Adaptive gain for K_{STAB}.

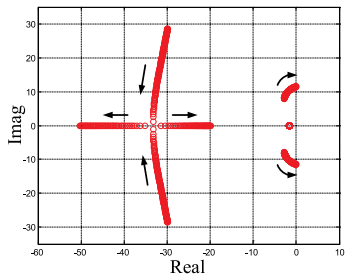

Fig. 10. Locus of the first five dominant eigenvalues for the overall system model with only 66.66 Ω load: $-30 < K_{STAB} < 10$.

In this system, P_{out} is from 0% to ±100%, thus K_{PE} is also from 0% to ±100% of its maximum value based on (13). K_{STAB} will be hard to design. To solve this problem, an adaptive gain is proposed for K_{STAB} in this paper, shown as Fig. 9. According to (13), K_{PE} is proportional to P_{out} when E is constant and the line impedance is inductive, so P_{out} is adopted to adjust K_{STAB}. This gain is like a proportional controller with saturations, and can prevent possible oscillations when the system transits between the generator and motor modes. The disadvantage is that, $G_{pss}(s)$ will have nearly no effect when P_{out} is zero, which is the worst condition as analyzed above. That is one of the reasons why a large m_{vdc} is chosen. In other words, $G_{pss}(s)$ is an auxiliary method to enhance the stability at high output power.

There are eight eigenvalues for the overall system model from (8)–(15), (18), and (22)–(24). Fig. 10 shows the locus of the first five dominant eigenvalues, while only a 66.66 Ω resistance load is connected to the VSMBI, and K_{PE} is negative. This verifies that, $G_{pss}(s)$ really has damping effect and can enhance the stability for the integrated system, when the VSMBI is working at high power. It also shows that, when the signs of K_{STAB} and K_{PE} are opposite, $G_{pss}(s)$ will degrade the stability.

IV. Simulation Verifications

Simulations using Simulink in MATLAB and PLECS are carried out on the single-machine infinite bus system shown in Fig. 1 with the default parameters in Table I, to verify the proposed concept and its VSM functions. Thus, the results related to the power electronics control, such as the detailed dc voltage ripple, are not shown [3], [7]. These performances are

$$\frac{\Delta\omega}{\Delta v_{dc\_R}} = \frac{-[C_{dc}V_{dc}s - G_{P\_dcmg}(s)]s}{[C_{dc}V_{dc}s - G_{P\_dcmg}(s)](J_{vir}s + m_\omega)s + K_{pss}G_{pss}(s)s + G_{LPF1}(s)K_{P\delta}} \tag{25}$$

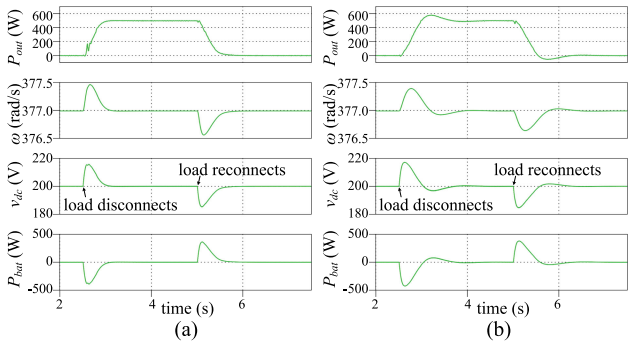

Fig. 11. Simulation results of *Case I*: (a) $J_{vir} = 1.06$ and (b) $J_{vir} = 4.24$.

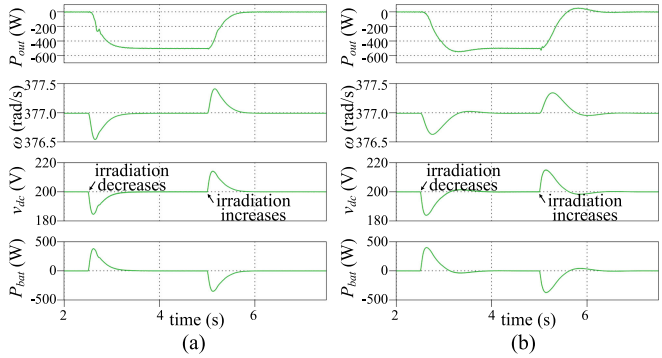

Fig. 12. Simulation results of *Case II*: (a) $J_{vir} = 1.06$ and (b) $J_{vir} = 4.24$.

traditional, and fast enough compared to those under the frequency regulation in Fig. 2(b) during the dynamics. The results about the ac voltage amplitude E are not shown either, because the control on E is just a traditional V-Q droop [3]–[5]. In the simulations, 500 W PV unit and 80 Ω resistance dc load are connected as default, and the SOC of batteries will not reach the boundary.

A. Case I

In this case, the ac grid works at constant 120 VAC/60 Hz. The 80 Ω load disconnects from the dc microgrid first, and then reconnects. Fig. 11 shows the results when J_{vir} is separately set at 1.06 and 4.24. The 120 Hz dc voltage ripple is hard to indicate in these and the following simulation results, because the time scale in the figures is set in second, to show the VSM functions. The ripple can be seen as "compressed" to a line with different "weights." In Fig. 11, after load disconnection, only PV unit and battery unit are connected, the VSMBI will work in generator mode. Though the changes in dc load are instantaneous, the proposed system still takes about 1.5 and 1.4 s to reach new working points of ω, v_{dc}, and P_{out} in Fig. 11(a), compared with 2.4 and 2.2 s in Fig. 11(b).

These results verify that, this system can output any power when ω_g is constant. When the dc load steps up and down quickly, the VSMBI can slow its own ω and P_{out}, according to J_{vir} and with the support from P_{bat}, and thus decouple its output dynamics from the dc microgrid. Indeed, the dynamic of P_{in} is also slowed by P_{bat}. The VSMBI with the dc microgrid really develops the swing characteristic as a SM. In Fig. 11, the total output energy from the battery unit is very small during the dynamics, so small energy rating batteries can be used here.

B. Case II

In this case, the ac grid works at constant 120 VAC/60 Hz. P_{PV} from the PV unit changes from 500 to 0 W first, and then changes back. Fig. 12 shows the results when J_{vir} is separately set at 1.06 and 4.24. The system takes about 1.3 and 1.2 s to reach new stable working points in Fig. 12(a), compared with 2.2 and 2.3 s in Fig. 12(b). The same functions of the proposed concept with *Case I* when the VSMBI works in motor mode and the dc source changes quickly are verified.

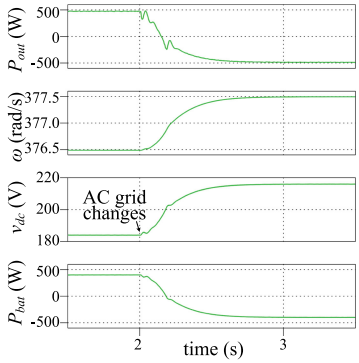

Fig. 13. Simulation results of *Case III*.

C. Case III

Fig. 13 shows the results when the ac grid changes from 115 VAC/59.92 Hz to 125 VAC/60.08 Hz at 2 s. In Fig. 13, the transition takes about 1.2 s. v_{dc} works at 184 V before the transition and 216 V after it, the dc load power is 423.2 and 583.2 W, respectively. The power from the battery unit is nearly 400 and –400 W due to the second droop, so P_{out} is about 476.8 and –483.2 W, as shown in Fig. 13.

These results verify that, the proposed concept can achieve the power management of the ac grid and dc microgrid simultaneously, when the ac grid is connected. They also show the swing characteristic of the proposed system during the dynamics. Moreover, the system can synchronize with the grid based on the power balance, and provide up-reserve and down-reserve to it when the ac grid works at desirable region in steady state. With the results in *Case I* and *II*, the integration of the DERs, loads, and energy storages in the dc microgrid into a VSM is achieved. In this case, batteries will keep charging or discharging to support the long-term reserves, when ω_g is not at its rated value, as shown in Fig. 13. So the batteries' energy rating will be determined by the long-term reserve requirement, and larger than that in *Case I* and *II*.

D. Case IV

In this case, at first the ac grid is disconnected, the VSMBI stops working while the dc microgrid keeps working. This transition is traditional and not shown here. Fig. 14(a) shows

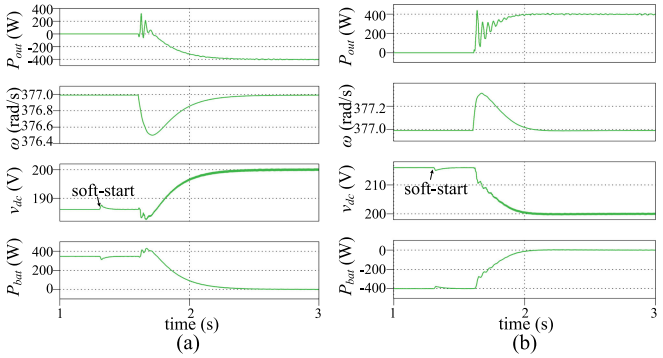

Fig. 14. Simulation results of *Case IV*: (a) reconnecting with battery unit and load and (b) reconnecting with battery unit and PV unit.

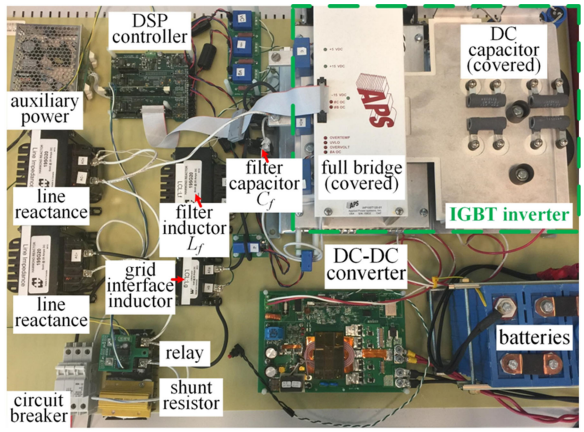

Fig. 15. Prototype of the single-machine infinite bus system.

the transition for the system reconnecting and synchronizing with the ac grid when only battery unit and 100 Ω load are connected, and Fig. 14(b) shows the transition when only battery unit and 400 W PV unit are connected.

Before reconnecting, P_{bat} is about 346 and –400 W, and v_{dc} is about 186.2 and 216 V, respectively in Fig. 14(a) and (b). The dc voltage is supported by the battery unit, and this verifies the achievement of the power management in dc microgrid when the VSMBI is not grid-connected.

To decrease the transient currents and voltages, soft-start mode should be added. After 0.3 s from the ac grid recovering point (at 1 s in Fig. 14), the PWM of the VSMBI is on and its ac output current is controlled to be zero under traditional power electronics control. So the overshoots in v_{dc} at 1.3 s are small in Fig. 14. Then after 0.3 s, the synchronization process starts. In the VSMBI, ω and δ are its internal control variables, so they can start from any values, different from the continuously running SM rotor. In this paper, a one-time use PLL is adopted to obtain ω_g and δ_g. It is just used for initializing ω and δ to ω_g and δ_g at the reconnecting point (at about 1.6 s in Fig. 14 when $\delta_g = \pi/2$ is chosen), similar to the frequency restoration in SM before grid connection [20]. After that, this PLL is eliminated from the control loop. The synchronizing transient performance will be controlled by the frequency and Volt–Var regulations. It takes about 1.3 and 1.2 s, respectively, as shown in Fig. 14. The regulations' starting from standing-by also causes some vibrations in P_{out}. The proposed concept's synchronization capability based on the power balance is verified.

V. Experimental Verifications

A prototype of the single-machine infinite bus system under the proposed concept is developed using a commercial, flexible, and highly integrated IGBT inverter, and its control is implemented in DSP TMS320F28335 with self-developed control board, shown as in Fig. 15. The dual active bridge circuit in [26] and [27] is chosen for the dc–dc converter in the battery unit. In the experiments, to emulate the quick power change in the PV unit, it is replaced by a programmable dc source, which works as a 2.5 A current source in default. The system stability is degraded, and experiments are carried out in this condition to

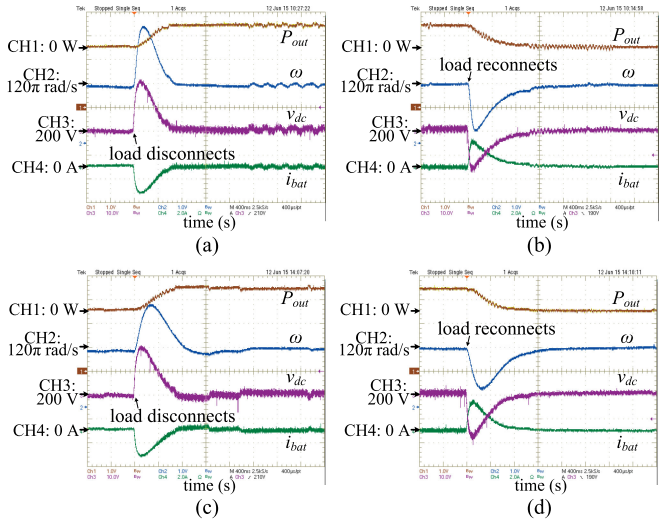

Fig. 16. Experimental results of *Case I*: (a) $J_{vir} = 1.06$, 80 Ω load changes to no load; (b) $J_{vir} = 1.06$, no load changes to 80 Ω load; (c) $J_{vir} = 4.24$, 80 Ω load changes to no load and (d) $J_{vir} = 4.24$, no load changes to 80 Ω load. CH1: P_{out} (500 W/div); CH2: ω (0.08 π rad/ s/ div); CH3: v_{dc} (10 V/ div); CH4: i_{bat} (2 A/ div); *X*-axis: time *t* (400 ms/ div).

demonstrate stability improvements discussed above. The other system setup and parameters are the same with the simulation conditions. The IGBT inverter is integrated with three-phase bridge and dc capacitor, while only full bridge is used for quick setup in this paper. Limited by the available dc source and the batteries, the prototype power rating is set as shown in Table I, with the IGBT inverter over-sized for this application. In the following results, i_{bat} is the current from the battery unit, and is positive when charging C_{dc}. The VSMBI's internal ω is made available through a digital-to-analog IC by the DSP, as well as P_{bat}.

A. Case I

In this case, the 80 Ω resistance load disconnects first, and then reconnects. Fig. 16 shows the results when J_{vir} is separately set at 1.06 and 4.24. The system will take about 1.7 and 2 s to reach

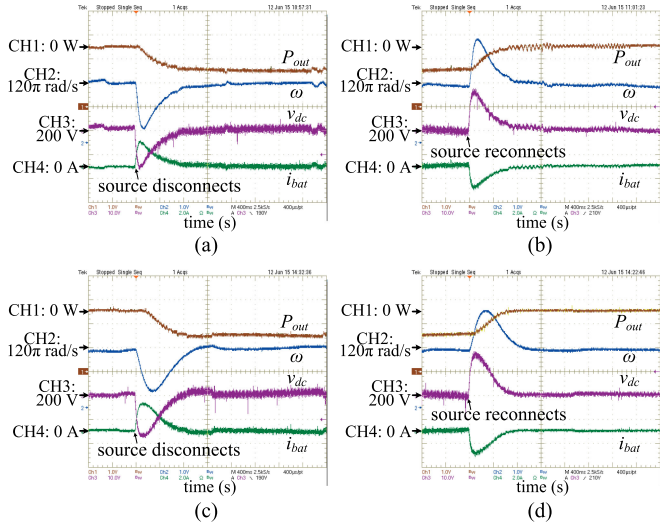

Fig. 17. Experimental results of *Case II*: (a) $J_{vir} = 1.06$, 2.5 A source changes to 0 A; (b) $J_{vir} = 1.06$, 0 A source changes to 2.5 A; (c) $J_{vir} = 4.24$, 2.5 A source changes to 0 A and (d) $J_{vir} = 4.24$, 0 A source changes to 2.5 A. CH1: P_{out} (500 W/ div); CH2: ω (0.08 π rad/ s / div); CH3: v_{dc} (10 V/ div); CH4: i_{bat} (2 A/ div); *X*-axis: time *t* (400 ms/ div).

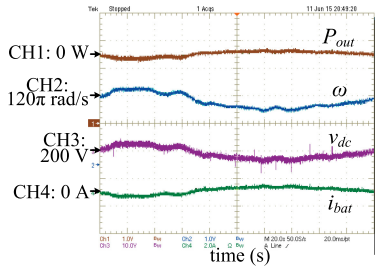

Fig. 18. Experimental results of *Case III*: CH1: P_{out} (500 W/ div); CH2: ω (0.08 π rad/ s / div); CH3: v_{dc} (10 V/div); CH4: i_{bat} (2 A/div); *X*-axis: time *t* (20 s/ div).

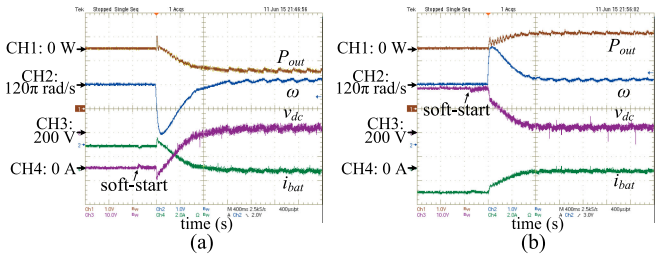

Fig. 19. Experimental results of *Case IV*: (a) reconnecting with battery unit and load and (b) reconnecting with battery unit and current source. CH1: P_{out} (500 W/div); CH2: ω (0.08 π rad/ s / div); CH3: v_{dc} (10 V/ div); CH4: i_{bat} (2 A/ div); *X*-axis: time *t* (400 ms/ div).

new working points in Fig. 16(a) and (b), compared with 2 and 2.1 s in Fig. 16(c) and (d). These results verify the effectiveness and functions of the VSMBI with the dc microgrid in generator mode, corresponding with *Case I* in simulation results.

In Fig. 16, ω and v_{dc} have small oscillations, and the frequency of these oscillations is random and much lower than 60 Hz. This is because the system is connected to the actual utility grid in the experiments, not an infinite ac bus in the simulations. In utility grid, the low-frequency interarea oscillations are quite normal, and usually from 0.1 to 2 Hz [20]. They will obviously cause the internal ω of the VSMBI to oscillate. To suppress these oscillations, the damping effects in the system could be enlarged by adding larger energy storage units and/or increasing the gain of $G_{pss}(s)$.

B. Case II

In this case, the dc source output current changes from 2.5 to 0 A first, and then changes back. Fig. 17 shows the results when J_{vir} is set at 1.06 and 4.24. The system takes about 1.6 and 1.2 s to reach new stable working points in Fig. 17(a) and (b), compared with 2.6 and 2 s in Fig. 17(c) and (d). The system's functions in motor mode are verified.

In Figs. 16 and 17, the "compressed" v_{dc} line with different "weights" is obvious. When the VSMBI outputs higher power, the line "weight" will be heavier, which indicates that the dc voltage ripple is larger.

C. Case III

Fig. 18 shows the results for 200 s when everything is in default setting. In Fig. 18, ω varies with the time, because ω_g is varying and ω is synchronizing with it. This small variation in ω_g is also normal in actual utility grid [20], and it is the reason why sometimes ω and v_{dc} do not work at the rated values in Figs. 16 and 17. Since the proposed system can synchronize its own frequency with ω_g in a high degree of accuracy, it can also work as a phasor measurement unit in the power systems.

In Fig. 18, v_{dc} and i_{bat} vary and follow ω according to the dual droop control. This verifies the effectiveness and functions of the dual droop control in the proposed concept, corresponding with *Case III* in simulation results.

D. Case IV

In this case, at first the ac grid is disconnected, the VSMBI stops working and the dc microgrid keeps working. Fig. 19(a) shows the transition for the system reconnecting and synchronizing with the ac grid when only battery unit and 100 Ω load are present, and Fig. 19(b) shows the transition when only battery unit and 2 A dc source are present.

Initially, i_{bat} is about 1.95 and –2.1 A, respectively, and v_{dc} is about 185.5 and 218.5 V; the system takes about 1.4 and 1.3 s to reconnect, as shown in Fig. 19. The achievement of power management in dc microgrid when the VSMBI is not working, and the proposed concept's synchronization capability are verified, corresponding with *Case IV* in simulation results.

E. Case V

In this case, only 66.66 Ω dc load is connected to the VSMBI. Fig. 20 shows the results when the control strategy is with and without $G_{pss}(s)$. The peak-to-peak values of the oscillations in ω with $G_{pss}(s)$ are obviously smaller in Fig. 20(a) than that without $G_{pss}(s)$ in Fig. 20(b). This shows that $G_{pss}(s)$

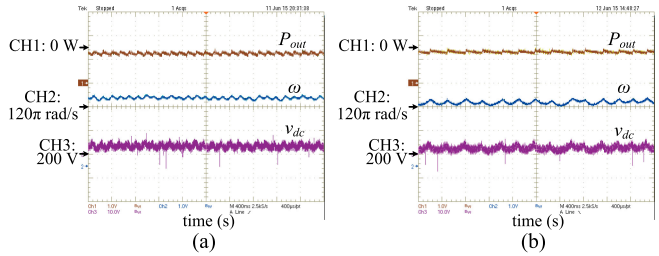

Fig. 20. Experimental results of *Case V*: (a) with $G_{pss}(s)$; (b) without $G_{pss}(s)$. CH1: P_{out} (500 W/ div); CH2: ω (0.08 π rad/ s/ div); CH3: v_{dc} (10 V/ div); CH4: i_{bat} (2 A/ div); *X*-axis: time *t* (400 ms/ div).

really has a damping effect and can suppress the low-frequency oscillations, when the system works at certain power outputs.

VI. Conclusion

This paper has proposed a comprehensive integration concept for dc microgrids into the legacy ac grid based on the VSM concept. It includes an improved frequency regulation and a dual droop control, and will obtain the following benefits:

1) integrate DERs, loads, and energy storages in the dc microgrid into a VSM;
2) achieve power management for the ac grid and dc microgrid, and enable the DERs and loads to output any power at a given ac frequency; and
3) introduce inertia, provide up-reserve and down-reserve for the grid with support from practical energy storages, and decouple the ac output from the fast responding DERs and loads.

Therefore, this concept is smart for integrating high penetration of DERs into the grid. The system modeling under this concept is proposed, and optimized methods, which include a newly introduced PSS applying to any VSMs, are developed. Finally, the simulation and experimental results verify the effectiveness and benefits.

References

[1] F. Katiraei and M. R. Iravani, "Power management strategies for a microgrid with multiple distributed generation units," *IEEE Trans. Power Syst.*, vol. 21, no. 4, pp. 1821–1831, Nov. 2006.

[2] N. Pogaku, M. Prodanovic, and T. C. Green, "Modeling, analysis and testing of autonomous operation of an inverter-based microgrid," *IEEE Trans. Power Electron.*, vol. 22, no. 2, pp. 613–625, Mar. 2007.

[3] M. Ashabani and Y. A.-R. I. Mohamed, "Novel comprehensive control framework for incorporating VSCs to smart power grids using bidirectional synchronous-VSC," *IEEE Trans. Power Syst.*, vol. 29, no. 2, pp. 805–814, Mar. 2014.

[4] M. Ashabani and Y. A.-R. I. Mohamed, "Integrating VSCs to weak grids by nonlinear power damping controller with self-synchronization capability," *IEEE Trans. Power Syst.*, vol. 29, no. 2, pp. 805–814, Mar. 2014.

[5] S. M. Ashabani and Y. A.-R. I. Mohamed, "New family of microgrid control and management strategies in smart distribution grids—Analysis, comparison and testing," *IEEE Trans. Power Syst.*, vol. 29, no. 5, pp. 2257–2269, Sep. 2014.

[6] Q.-C. Zhong and G. Weiss, "Synchronverters: Inverters that mimic synchronous generators," *IEEE Trans. Ind. Electron.*, vol. 58, no. 4, pp. 1259–1267, Apr. 2011.

[7] Q.-C. Zhong, P.-L. Nguyen, Z. Ma, and W. Sheng, "Self-synchronized synchronverters: Inverters without a dedicated synchronization unit," *IEEE Trans. Power Electron.*, vol. 29, no. 2, pp. 617–630, Feb. 2014.

[8] H. Wu *et al.*, "Small-signal modeling and parameters design for virtual synchronous generators," *IEEE Trans. Ind. Electron.*, vol. 63, no. 7, pp. 4292–4303, Jul. 2016.

[9] M. F. M. Arani and E. F. El-Saadany, "Implementing virtual inertia in DFIG-based wind power generation," *IEEE Trans. Power Syst.*, vol. 28, no. 2, pp. 1373–1384, May 2013.

[10] J. Zhu, C. D. Booth, G. P. Adam, A. J. Roscoe, and C. G. Bright, "Inertia emulation control strategy for VSC-HVDC transmission systems," *IEEE Trans. Power Syst.*, vol. 28, no. 2, pp. 1277–1287, May 2013.

[11] J. Liu, Y. Miura, and T. Ise, "Comparison of dynamic characteristics between virtual synchronous generator and droop control in inverter-based distributed generators," *IEEE Trans. Power Electron.*, vol. 31, no. 5, pp. 3600–3611, May 2016.

[12] S. D'Arco, J. A. Suul, and O. B. Fosso, "Small-signal modelling and parametric sensitivity of a virtual synchronous machine," in *Proc. Power Syst. Comput. Conf.*, Aug. 2014, pp. 1–9.

[13] F. Guo, C. Wen, J. Mao, and Y. Song, "Distributed secondary voltage and frequency restoration control of droop-controlled inverter-based microgrids," *IEEE Trans. Ind. Electron.*, vol. 62, no. 7, pp. 4355–4364, Jul. 2015.

[14] X. Lu, K. Sun, J. M. Guerrero, J. C. Vasquez, and L. Huang, "State-of-charge balance using adaptive droop control for distributed energy storage systems in dc microgrid applications," *IEEE Trans. Ind. Electron.*, vol. 61, no. 6, pp. 2804–2815, Jun. 2014.

[15] J. C. Vasquez, G. M. Guerrero, M. Savaghebi, J. Eloy-Garcia, and R. Teodorescu, "Modeling, analysis, and design of stationary-reference-frame droop-controlled parallel three-phase voltage source inverters," *IEEE Trans. Ind. Electron.*, vol. 60, no. 4, pp. 1271–1280, Apr. 2013.

[16] G. M. Guerrero, J. C. Vasquez, J. Matas, L. G. de Vicuna, and M. Castilla, "Hierarchical control of droop-controlled ac and dc microgrids—A general approach toward standardization," *IEEE Trans. Ind. Electron.*, vol. 58, no. 1, pp. 158–172, Jan. 2011.

[17] S. Eren, M. Pahlevani, A. Bakhshai, and P. Jain, "An adaptive droop dc-bus voltage controller for a grid-connected voltage source inverter with LCL filter," *IEEE Trans. Power Electron.*, vol. 30, no. 2, pp. 547–560, Feb. 2015.

[18] P. C. Joh, D. Li, Y. K. Chai, and F. Blaabjerg, "Autonomous control of interlinking converter with energy storage in hybrid ac-dc microgrid," *IEEE Trans. Ind. Appl.*, vol. 49, no. 3, pp. 1374–1382, May/Jun. 2013.

[19] P. C. Joh, D. Li, Y. K. Chai, and F. Blaabjerg, "Autonomous operation of hybrid microgrid with ac and dc subgrids," *IEEE Trans. Power Electron.*, vol. 28, no. 5, pp. 2214–2223, May 2013.

[20] P. Kundur, *Power System Stability and Control*. New York, NY, USA: McGraw-Hill, 1994, pp. 128–136, 581–592, 699–822.

[21] L. Zhang, L. Harnefors, and H.-P. Nee, "Interconnection of two very weak ac systems by VSC-HVDC links using power-synchronization control," *IEEE Trans. Power Syst.*, vol. 26, no. 1, pp. 344–355, Feb. 2011.

[22] S. D'Arco, J. A. Suul, and O. B. Fosso, "Control system tuning and stability analysis of virtual synchronous machines," in *Proc. IEEE Energy Convers. Congr. Expo.*, Sep. 2013, pp. 2664–2671.

[23] N. S. Nise, *Control System Engineering*, 6th ed. Hoboken, NJ, USA: Wiley, 2010, pp. 162–195.

[24] D. Chen, A. Q. Huang, Y. Xu, F. Wang, and W. Yu, "Distributed and autonomous control of the FREEDM system: A power electronics based distribution system," in *Proc. 40th Annu. Conf. IEEE Ind. Electron. Soc.*, Dallas, TX, USA, 2014, pp. 4954–4960.

[25] Los Alamos National Laboratory. dc Microgrids Scoping Study: Estimate of Technical and Economic Benefits, Mar. 2015. [Online]. Available: http://energy.gov/oe/downloads/dc-microgrids-scoping-study-estimate-technical-and-economic-benefits-march-2015

[26] F. Krismer and J. W. Kolar, "Efficiency-optimized high-current dual active bridge converter for automotive applications," *IEEE Trans. Ind. Electron.*, vol. 59, no. 7, pp. 2745–2760, Feb. 2012.

[27] F. Xue, R. Yu, W. Yu, A. Q. Huang, and Y. Du, "A novel bi-directional dc-dc converter for distributed energy storage device," in *Proc. IEEE Appl. Power Electron. Conf. Expo.*, Charlotte, NC, USA, 2015, pp. 1126–1130.

Dong Chen was born in Luoyang, China. He received the B.Sc. and Ph.D. degrees in electrical engineering from Zhejiang University, Zhejiang, China, in 2006 and 2012, respectively.

Since 2013, he has been with North Carolina State University, Raleigh, NC, USA and is currently a Postdoctoral Researcher in the NSF FREEDM Systems Center. His current research interests include virtual synchronous machines, solid-state transformers, solar systems, microgrids, and related control technologies.

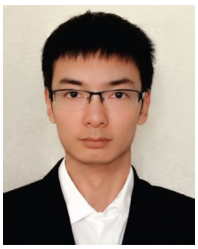

Yizhe Xu (S'12) was born in Harbin, China. He received the B.Sc. degree from Wuhan University, Wuhan, China, in 2010, and the M.Sc. degree from North Carolina State University, Raleigh, NC, USA, in 2012, both in electrical engineering. He is currently working toward the Ph.D. degree in electrical engineering at the FREEDM Systems Center, North Carolina State University, where he has been a Research Assistant since 2010.

His research interests include power electronics converter control, solid-state transformers, virtual synchronous machines, integration of distributed renewable energy resources, and microgrid system control and power management.

Alex Q. Huang (S'91–M'94–SM'96–F'05) was born in Zunyi, China. He received the B.Sc. degree from Zheijiang University, Hangzhou, China, in 1983, and the M.Sc. degree from the Chengdu Institute of Radio Engineering, Chengdu, China, in 1986, both in electrical engineering. He received the Ph.D. degree in electric engineering from Cambridge University, Cambridge, U.K., in 1992.

From 1992 to 1994, he was a Research Fellow at Magdalene College, Cambridge, U.K. From 1994 to 2004, he was a Professor with the Bradley Department of Electrical and Computer Engineering, Virginia Polytechnic Institute and State University, Blacksburg, VA, USA. Since 2004, he has been with North Carolina State University (NCSU), Raleigh, NC, USA, and is currently the Progress Energy Distinguished Professor of Electrical and Computer Engineering. He established the NSF FREEDM Systems Center at NCSU in 2008. Since 1983, he has been involved in the development of modern power semiconductor devices and power integrated circuits. He fabricated the first IGBT power device in China in 1985. He is the inventor and key developer of the emitter turn-off (ETO) thyristor technology. He developed the concept of Energy Internet and the key smart transformer-based Energy Router technology. His current research interests are power electronics, power management microsystems, and power semiconductor devices. He has mentored and graduated more than 70 Ph.D. and Master's students, and has published more than 450 papers in international conference proceedings and journals. He has also been granted more than 20 U.S. patents.

Prof. Huang received a National Science Foundation CAREER Award, the prestigious R & D 100 Award, and the *MIT Technology Review* 2011 Technology of the Year Award.